Journal Pre-proof

Measurement and FEM of ice adhesion to the downstream pipe of an air cycle machine

An Feng, Abhay Vincent, M.L.A. Pervier

PII: S0165-232X(22)00031-3

DOI: https://doi.org/10.1016/j.coldregions.2022.103512

Reference: COLTEC 103512

To appear in: *Cold Regions Science and Technology*

Received date: 16 August 2021

Revised date: 22 January 2022

Accepted date: 3 February 2022

Please cite this article as: A. Feng, A. Vincent and M.L.A. Pervier, Measurement and FEM of ice adhesion to the downstream pipe of an air cycle machine, *Cold Regions Science and Technology* (2021), https://doi.org/10.1016/j.coldregions.2022.103512

This is a PDF file of an article that has undergone enhancements after acceptance, such as the addition of a cover page and metadata, and formatting for readability, but it is not yet the definitive version of record. This version will undergo additional copyediting, typesetting and review before it is published in its final form, but we are providing this version to give early visibility of the article. Please note that, during the production process, errors may be discovered which could affect the content, and all legal disclaimers that apply to the journal pertain.

© 2022 Published by Elsevier B.V.

Journal Pre-proof

Cold Regions Science and Technology, Volume 196, April 2022, Article number 103512
DOI:10.1016/j.coldregions.2022.103512

Measurement and FEM of Ice Adhesion to the Downstream Pipe of an Air Cycle Machine

An Feng [a,b,*], Abhay Vincent [b], ML.A. Pervier [b]

[a] AECC Hunan Aviation Powerplant Research Institute, Zhuzhou, China

[b] Cranfield University, Cranfield MK43 0AL, UK

Abstract

Ice accretion on the downstream pipe of an air cycle machine can lead to pipe blockage and turbine blade damage, and therefore de-icing is needed. Most previous studies focused on ice shedding from flat surfaces, and average interface shear strength rather than the true shear strength was usually reported. Here, the debonding of the interface between ice and cylindric surfaces of an aluminium pipe (2024-T3) was studied trying to understand the mechanism of interface fracture and to obtain the true adhesive shear strength and fracture energy. Average adhesive strength was measured first in the scrape test and the result was used to calibrate the finite element analysis. A cohesive zone model (CZM) with bilinear traction-separation law was used to simulate the interface delamination. The true shear strength σ_{cs} and mode-II

* Corresponding author.

E-mail address: buaafengan@qq.com ; Phone number: +86 18153812709

Published by Elsevier. This is the Author Accepted Manuscript issued with: Creative Commons Attribution Non-Commercial No Derivatives License (CC:BY:NC:ND 4.0). The final published version (version of record) is available online at DOI:10.1016/j.coldregions.2022.103512. Please refer to any applicable publisher terms of use.

energy release rate G_{cs} were determined by matching the numerically predicted critical force to the measured force. The influence of shear strength and shear energy release rate on the critical force was also investigated. At the interface, both the damage factor and the peak shear stress were found progressing away from the edge as the pushing force increased. Parametric studies on the influence of the length of the interface was performed. The critical force first increased and then stabilised with the increase of the length, showing the same trend as that of a theoretical model which ignored the mode-I fracture.

Keywords

Air cycle machine; Ice adhesion; Finite element analysis; Cohesive zone model; Shear strength; Energy release rate

Nomenclature

	Interface contact area
ACM	Air cycle machine
CZM	Cohesive zone model
	Young's modulus
	Pushing force
$\dot{F}$	Change rate of the pushing force

$\widetilde{\Delta F}$	Threshold for the difference between FEA and measured value of the critical force
$_c$	Critical force to remove ice from pipe
$_{c,avg}$	Average critical force to remove ice from pipe
FEA	Finite Element Analysis
FEM	Finite Element Modelling
G_c	Critical energy release rate
G_{cs}	Critical shear (mode II) energy release rate
G_c	Critical tensile (mode I) energy release rate
	Thickness of the ice block
LWC	Liquid water content
	Length of the ice block
$_c$	Critical length beyond which the interface debonding becomes toughness-controlled
MVD	Mean volume diameter
	$_c$, critical force per unit width
	Time
	Time of shedding moment
	Displacement

$_c$	Critical displacement (beyond which damage will be induced)
	Fracture displacement
	Width of the ice block
XFEM	Extended Finite Element Method
ZDCT	Zero-degree cone test
	Poisson's ratio
	Density
σ_c	Critical stress (strength)
σ_{cs}	Shear (mode II) strength
σ_{cs}	Average shear strength
σ_c	Tensile (mode I) strength

1 Introduction

Aircraft icing poses a hazardous threat to aviation safety. In a typical flight envelop, an aircraft can suffer from different types of icing issues, such as ground icing and in-flight impact icing. Ice accretion on wings, fuselages and nacelles have been intensively studied and their detrimental impacts have been widely recognised [1][2][3]. Inside the aircraft, icing can be a serious problem too, as this can be found at the downstream pipe of the expansion turbine of an air cycle machine (ACM).

The ACM is an important part of the aircraft environmental control system. It bleeds air from the engine using it for purposes of cabin air-conditioning and electronical equipment cooling. Fig. 1 shows the main stages air goes through in a typical ACM. Ice accretion occurs at the pipe exit to the turbine as the air expands rapidly, accompanying a sharp drop in its temperature (Fig. 2). The accumulation of ice can lead to pipe blockage and turbine blades damage, and thus de-icing is necessary.

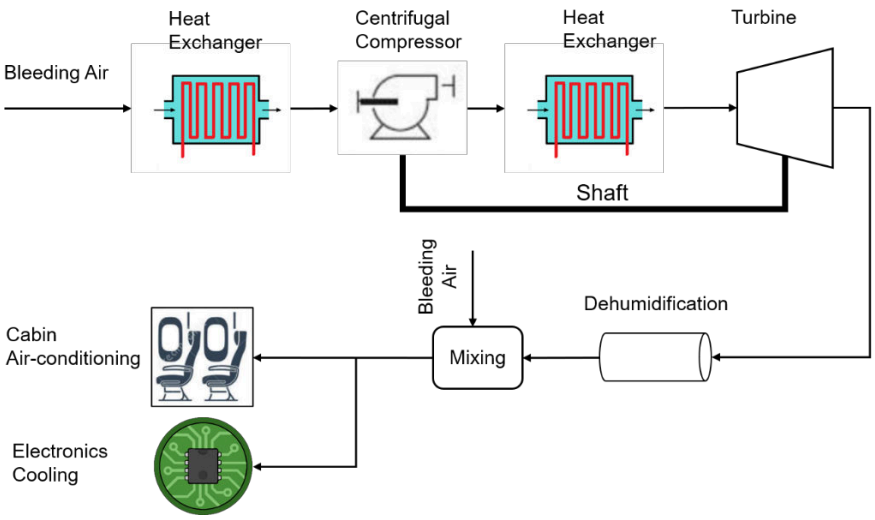

Fig. 1 The cycle air goes through in a typical air cycle machine

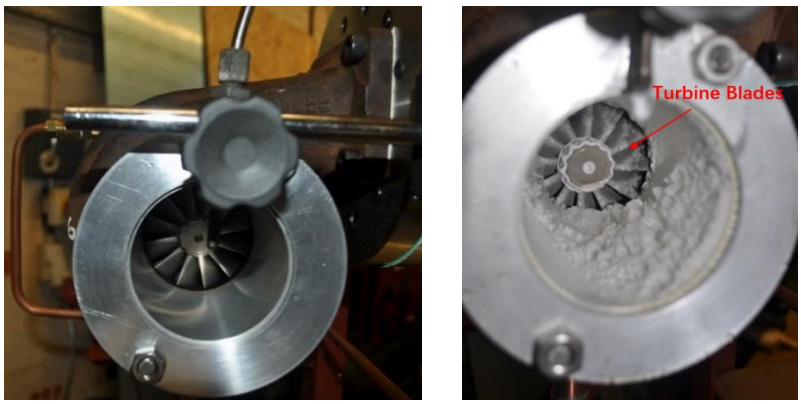

(a) Before start (b) A few minutes after start

Fig. 2 Ice accretion at the downstream pipe of an expansion turbine. A thick layer of ice has accreted on the surface of the pipe and blades just a few minutes after the start of the turbine

The ice adhesion to pipe must be studied first if a more efficient way of de-icing is targeted. Over the years, a number of tests have been designed to measure the shear force needed to break the interface of ice/substrate, which can be categorised as centrifugal, push and torsion tests [4]. For centrifugal tests, samples of ice and substrate are attached on revolving devices, and debonding occurs at high speed of rotation. The cohesive interface can either be flat [5][6][7] or curved mimicking the aircraft wing [8] or the rotor blade of a helicopter [9][10]. The shedding moment is usually captured by piezoelectric cells imbedded in the wall of the vat that holds the test sample [5][6], and the centrifugal force can thus be calculated. One possible problem facing centrifugal tests is that additional forces such as vibration and aerodynamic forces can influence the adhesion of ice and thus lead to inaccurate measurement [11]. Push tests are the most common ones which are characterised by directly applying forces to ice [11][12][13] or substrates [14][15], inducing shear forces at the interface that detaches the ice/substrate

bonding. Depending on the shape of contact surface between ice and substrates, push tests can be distinguished as direct lap-shear tests [13][16][17] and zero-degree cone test (ZDCT) [12][18], of which results are widely reported and compared. The set-up of the lap-shear test is straightforward: the rectangular ice block adheres to the substrate on the flat interface, and the push is exerted parallel to the interface on the side surface of the ice block. The ice/substrate interface in a ZDCT, however, is cylindrical, with ice adhering to the surface of a rod and force applied to the rod along its axis. The contact interface of torsion tests has a similar shape to that of ZDCT, but the force is applied as a torque rather than a push [8][19] [20]. Torsion tests were popular in last century but few people perform such tests nowadays.

A problem with the measurement of ice adhesive strength is that results reported by different authors vary [4]. For bare aluminium substrates, the highest values can be an order of magnitude higher than the lowest ones. There are many possible causes. One of them is the complicity of the ice/substrate interface. When ice is formed, air bubbles can be trapped inside and they coalesce with each other forming voids [21]. The voids can be the spots where cracks initiate, resulting in a drop in the measured adhesive shear strength. It is almost impossible to avoid air bubbles during ice accumulation, and the amount of air bubbles at ice interfaces may differ from one test to

another. Even if ideal bubble-free interfaces were achieved, microscopic crystal boundaries could be defects where potential crack initiation may take place [22][23][24][25]. Experiments have shown that icing conditions influence grain sizes and thus their boundaries [26]. In addition to this, surface conditions of substrates varied from test to test, which can be another reason for inconsistent results of shear strength [11][27]. Also, the mechanical properties of ice may depend on the icing condition and its accretion history. For impact ice, studies have shown that ambient temperature, liquid water content and wind velocity can affect both shear [11] and tensile [28] strength.

Apart from all the factors mentioned above, recent studies pointed out that the interfacial fracture in lap-shear and ZDCT tests was either strength-controlled or toughness-controlled, depending on the length of the interface [17][29]. For sufficiently long interfaces, the interfacial fracture is decided solely upon fracture energy and irrelevant to the adhesive shear strength. The fracture was actually controlled by fracture toughness for many previous ZDCT, and therefore the apparent ice adhesion strengths reported were not the true shear strength of ice/substrate interfaces [29]. The debonding of the interface should therefore be approached based on fracture mechanics. This approach is much different from the average-strength based analysis which determines the fracture of the interface following the criterion that the average shear stress

should exceed the interface's shear strength (usually the apparent shear strength measured from lap-shear or ZDCT tests).

Although it takes much effort to experimentally determine whether the fracture is controlled by interfacial toughness or strength, the separation of the interface can be more easily modelled numerically implementing cohesive zone model (CZM) which provides a way to relate stress, displacement and dissipation energy with fracture. To model decohesion using CZM, the crack path must be predefined, which is along the interface, and cohesive zone is assumed lying ahead the crack tip, as shown in Fig. 3. The traction-separation law specifies the amount of separation when the material inside the cohesive zone is subject to certain levels of stresses. The cohesive zone goes through two stages before it breaks: the first stage of linear elastic deformation (A to B) with no damage caused, followed by the second stage of softening (B to D) characterised by decreased material strength and increased damage. At the end of linear elastic stage, the stress reaches its maximum, which is the strength of the interface σ_c and can be considered as a material property. The gradient of AB is the stiffness of the interface, denoted by k. The area under the traction-separation curve is the fracture energy G_c – the amount energy dissipated in the process of crack opening. Separation will occur once the material is stressed, but in reality, the crack will not be initiated unless stress

exceeds the interfacial strength and all fracture energy is dissipated. This is the reason why the crack between A and D in Fig. 3 is noted as “fictitious crack” – it is not a real crack but appears as a crack in the numerical simulation due to the implication of CZM.

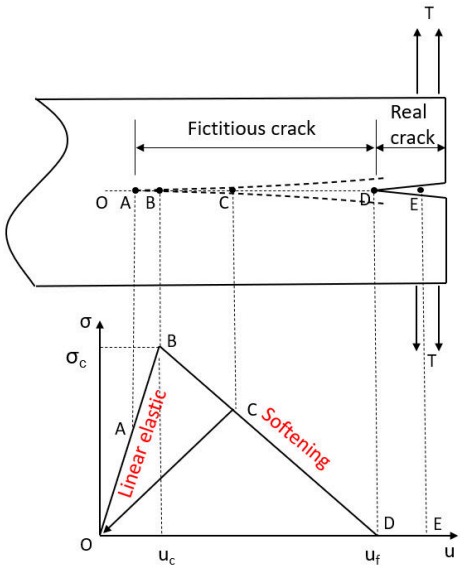

Fig. 3 Cohesive zone and the corresponding bilinear traction-separation curve.

Near the crack tip is the cohesive zone which governed by the traction-separation law. The schematic is illustrated in the fashion of mode-I fracture, but mechanisms are the same for mode-II fracture.

Successful application of CZM to predict the debonding of ice/substrate interfaces has been widely reported in the literature. Chen [30] studied the ice shedding from fan blades due to centrifugal forces. The numerical model ignored the possible mode-II failure of interface but took into account the vibration of the blade. However, a clear statement about the interface fracture

condition was not made in the paper, and the assumption for the cohesive fracture path was far from accurate. Subsequently, Fu [31] and Chen [32] improved their model by introducing the extended finite element method (XFEM) and an iterative method coupling stress, ice shape and crack propagation together, and used it to predict ice shedding from the inlet cone of an engine. Interestingly, CZM was introduced to study the influence of surface roughness on tensile strength of ice/aluminium interface [33]. Finite element analysis using CZM can be performed to study the stress distribution across the interface in both mode-I and mode-II interfacial delamination. Riahi et al. [34] combined the brittle cracking theory and cohesive material theory to study the de-icing of a thin aluminium slate under traction. They introduced cracking model to approximate the degradation in material's modulus after the crack was opened in the ice, while the interface was modelled by CZM with linear traction-separation law. The excellent agreement of numerical and experimental results indicated the potential of CZM in predicting the ice/aluminium interface separation. Schulz and Sinapius [35] evaluated the stress distribution at the interface for three common types of adhesion tests: lap-shear, bending and centrifugal. The study revealed that for lap-shear test, even if the force was applied parallel to the interface, it still induced tensile stresses, meaning that mode-I fracture should not be neglected in a mode-II-dominated fracture analysis. Pervier et al. [11] performed a finite

element study based on the result of an in-situ lap-shear test. By obtaining the longitudinal stress distribution and assuming that crack initiates from the edge, the authors managed to get the fracture toughness of the ice/titanium interface by extrapolating the stress intensity curve.

Most of the previous studies on mode-II fracture of ice/substrate interfaces focused on flat substrates or blades, and cylindrical interfaces inside a pipe have rarely been touched upon. Besides, few studies have approached this problem from the perspective of fracture mechanics which truly reflects the physics of debonding. The fracture energy and the true strength of the interface have rarely been reported. In this paper, the experiment which measures the shear strength of ice adhereing to the inner surface of a pipe will first be described and the result will be reported. Based on the experiment, the result of a finite element study which proposes an iterative way to obtain the fracture energy and shear strength will then be presented.

2 Experiment

The experiment was designed in a way trying to replicate the real icing conditions in an ACM so that adhesive shear strength measured would be close to the real de-icing stress. The experiment consisted of two stages: ice formation and scrape test. In stage 1, ice samples were made at controlled

conditions. Then, the ice sample was taken to stage 2 where the adhesive shear strength was measured by performing a scrape test.

2.1 Apparatus

A conceptual diagram illustrating the configuration of the stage-1 test rig is shown in Fig. 4. The rig was comprised of five sub-systems: a) air supply system, b) water supply system, c) mixing system, d) icing system, e) exhausting system. The function and structure of each sub-system were detailed in a conference paper by Vincent et al. [36]. Ice was formed on the inner surface of the aluminium pipe (aluminium 2024-T3) in the icing system. The inner diameter D_i, outer diameter D_o, and length of the pipe L were at 82.55 mm, 101.6 mm respectively. A Holset HX-35 turbocharger, with only the turbine part being used, functioned as a free expansion turbine. The mass flow of air and water supply can be accurately controlled to ensure the right humidity of the air entering the turbine.

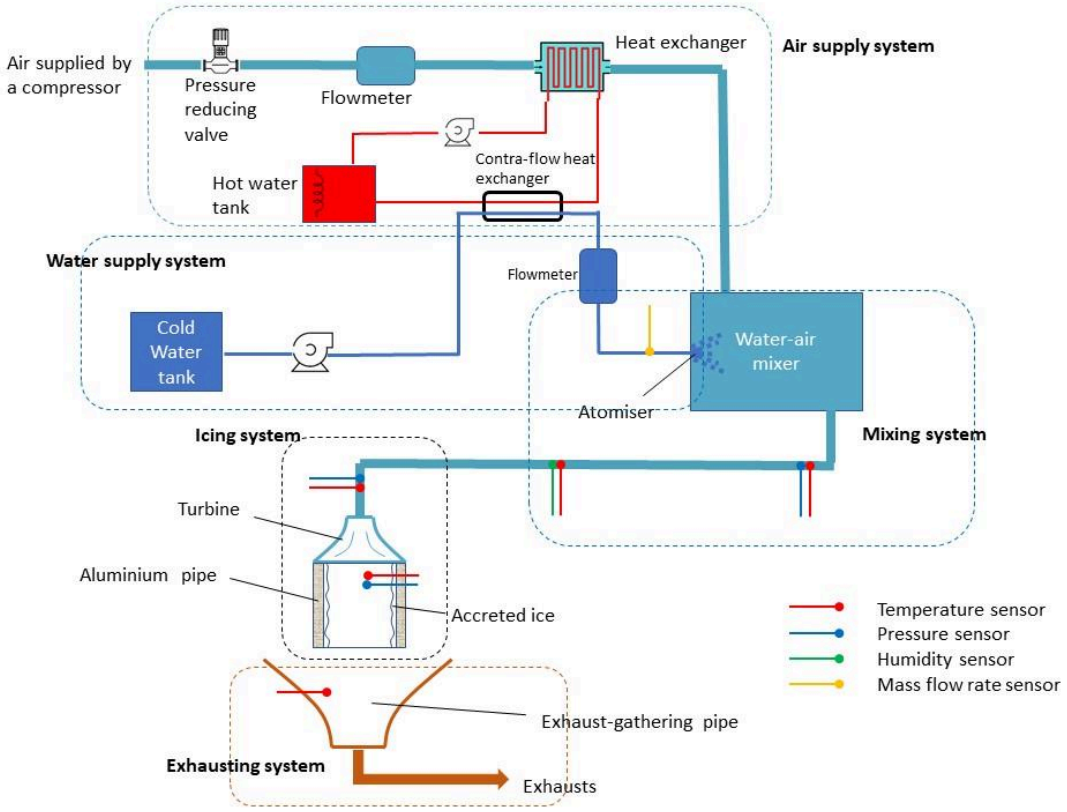

Fig. 4 Configurations of the stage-1 test rig. The rig is able to recreate icing conditions in a real ACM. Ice accretes on the inner surfaces of the aluminium pipe in the icing system. Where necessary, parameters such as pressures and temperatures were measured.

The design of the scrape adhesion test was inspired by the Balanced Beam Adhesion Testers commonly used in the paint and coating testing industry. The purpose of the test was to break the ice from the substrate in pure adhesive motion and minimise any peeling effects. To target on a full adhesive debonding, forces were applied to the scraper in the direction parallel to the interface, as shown in Fig. 5, pushing the ice block sample to break adhesively

from the aluminium pipe. the ice was scratched off from the pipe, and this is the reason why it is called “Scrape Test”.

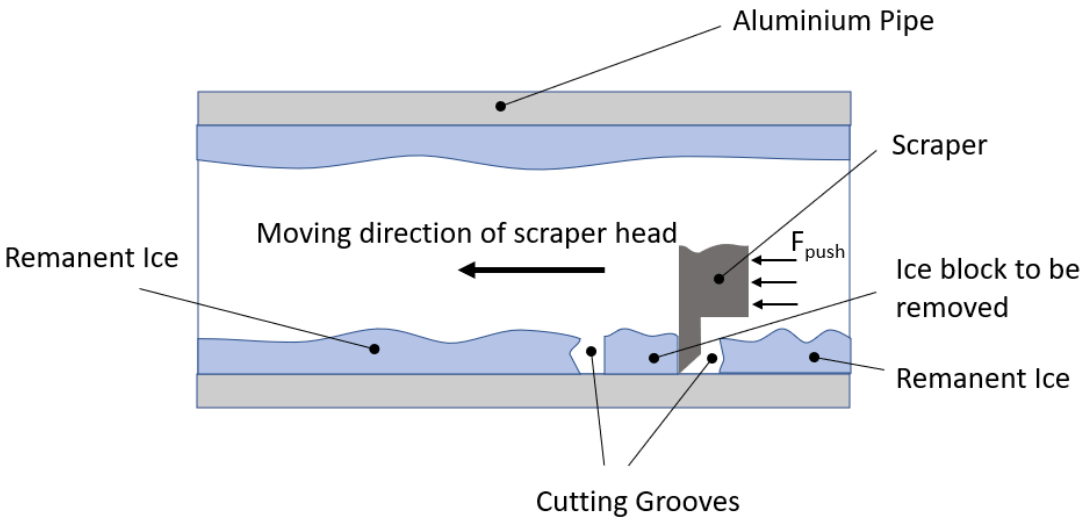

Fig. 5 A diagram illustrating the principle of the scrape test.

The configuration of the stage-2 test rig is shown in Fig. 6. Main components of the rig include a scraper to remove the ice block sample, a V-block to support the pipe, a load cell to measure the force, a pneumatic actuator to apply the push, and other supporting parts. The load cell was placed between the scraper and the pneumatic actuator when the test was ready to perform.

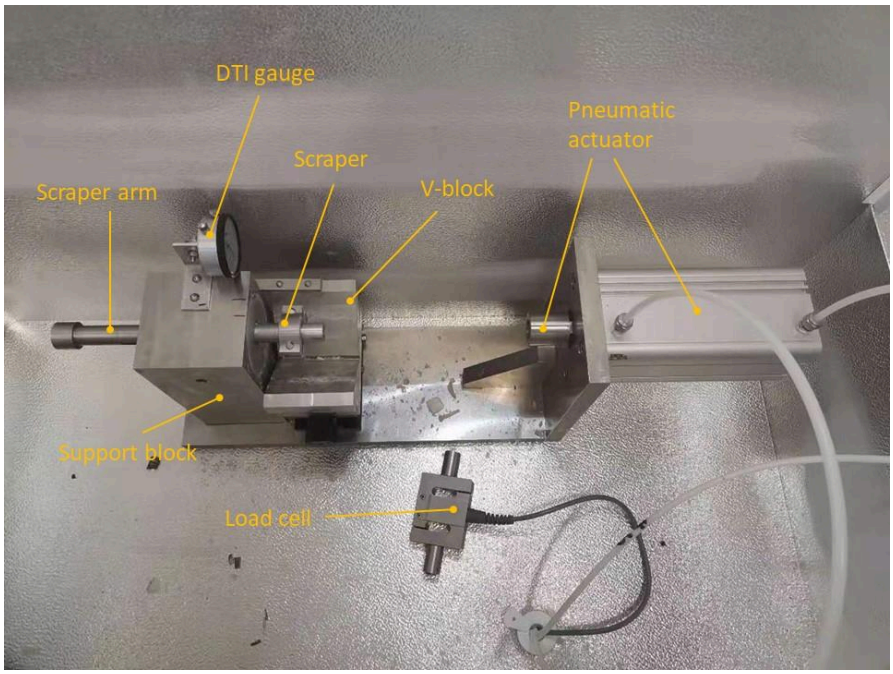

Fig. 6 Configurations of the stage-2 test rig (scrape test). The entire rig was placed in a freezer before and during the test to achieve a temperature balance

After ice sample was made in stage 1, it was immediately put in a freezer where stage-2 test was performed. A 2cm × 2cm ice block was cut from the ice sample using a metallic cutter heated up by a hot air gun. This was done in the freezer to minimise the melting of ice and resultant thermal stresses. To further reduce the influence of possible thermal stresses, the ice-pipe sample was left in the freezer untouched in the next 30 minutes so that any remaining thermal stresses were allowed to release. Next, the sample was placed on the V-block (Fig. 6) whose vertical position could be altered by adjusting the position of the scissors lift on which it was mounted. The transfer of the ice-pipe sample to the

freezer must be finished as quickly as possible to minimise the heat transfer that might impact the interfacial adhesive strength. Before testing, the V-block was adjusted carefully to the position just in contact with the scraper head, and then the vertical position of the V-block was noted by the help of a DTI gauge. Every time the test was to be performed, the scissors lift would firstly be adjusted to the pre-determined position and consequently the scraper head and the sample pipe would be just in contact with each other. One end of the pipe was against the support block preventing the pipe from moving axially during the test. The load cell was attached to the scraper arm to record the pushing force. It was connected to a PC running LabView allowing measured force values to be logged to a spreadsheet. The pneumatic actuator was attached to the other end of the load cell to apply the pushing force.

2.1 Test conditions

To allow for a successful scrape test, the ice sample must be adequately thick and uniform and firmly attached to the pipe. This requires suitable icing conditions. In the test, ice was produced at several different conditions but it was found that ice formed in the condition listed in Tab. 1 was most suitable for the scrape test.

Tab. 1 Test Conditions

Water temperature (ºC)	20
Water flow (L/min)	0.15
Air Mass Flow (kg/s)	0.39
Supply Air Pressure (bar)	3.96
Supply Air Temperature (ºC)	14.66
Air temperature after mixing (ºC)	12.56
Air Pressure after mixing (bar)	17.13
Air temperature before expanding (ºC)	1.71
Air Pressure before expanding (bar)	1.72
Exhaust temperature (ºC)	-18.49
Turbine rotational velocity (rpm)	60,000
Ice type	Rime ice

Ice accumulation time (min)	Approx. 6

2.2 Experimental results

The critical force is the force required to break the ice/pipe interface, and it was measured to be at 127 N. The average shear strength $\sigma_{cs,avg}$ can be determined by simply dividing the critical force (F_c) by the area of contact between the ice and the pipe, A.

$$\sigma_{cs} = \frac{c}{} = \frac{127N}{0.02m \times 0.02m} = 317.5\ kPa \quad (1)$$

The exhaust temperature, at -18.45 ºC, can be taken to be the temperature in the pipe. If the influence of the liquid water content (LWC) and the mean volume diameter (MVD) were neglected here, a rough comparison can be made with results found in the literature in terms of the shear strength of ice/aluminium interfaces. The current result was pretty close to that of Rønneberg et al. [37] which was measured from centrifugal tests, at 340 kPa (precipitation ice, -18 ºC) and 285 kPa (impact ice, -18 ºC), and to that of Druez et al. [12] that was obtained from push tests, at 325 kPa (impact ice, -18 ºC). Also, the current measured average strength was not far away from findings of Chu and Scavuzzo [38], at 381 kPa (impact ice, -17.6 ºC).

The increasing rate of the force applied can be obtained using the following equation:

$$\cdot = \frac{F_c - {}_0}{t_c - t_0} = \frac{127N - 0N}{10.6s - 10.2s} = 317.5\ N/s \quad (2)$$

where, subscript ‘c’ denotes the critical value (shedding point), ‘0’ denotes the starting point of force applied.

3 Numerical simulation

As discussed in the introduction, the average shear strength of ice/pipe interface measured in the experiment may not be the real adhesive shear strength σ_c. Based on the result of the experiment, the numerical simulation took a step further to find the true adhesive strength and fracture energy. The numerical study was performed on the commercial FEM code COMSOL Multiphysics 5.5.

3.1 FEA setup

Considering that both the geometry and physics were symmetric about XZ plane, only half of the pipe and ice block was modelled to bring down the computational time (see Fig. 7). In the experiment, pushing force (thick red arrow in Fig. 7) was applied via the scraper head to the side surface of the ice block in positive X direction. Since the scraper was nicely in touch with the ice

block so the push could be considered uniformly distributed across the surface it was acting on. Therefore, in FE model a surface pressure was applied to this surface to ensure a uniform distribution, with an equivalent increasing rate of $317.5\ N/s$, identical to the experiment. The pipe was placed on the top of the V-block with one end being against the support block, and therefore a fixed constraint – zero degree-of-freedom – was assigned to the bottom half and the end surfaces. A symmetry constraint was set to the central XZ plane, meaning that the y gradient for all parameters at the symmetric plane were zero.

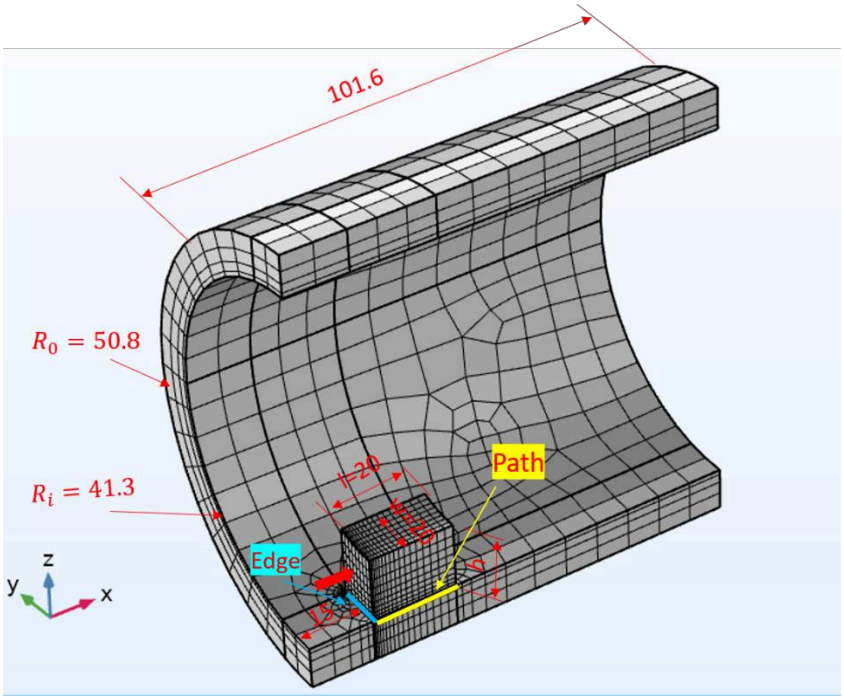

Fig. 7 Computational geometry and mesh. The path was taken at the midline of the interface, along which stresses were evaluated (unit: mm).

The ice/pipe interface was modelled using “contact node” available in COMSOL Multiphysics. Ice and the pipe were in contact during the entire

simulation and therefore the “always active” type was set for the adhesion sub-node. the stiffness of the contact surface was assigned to be $0.5 \times 10^{15}\ N/m^3$ for all three modes (mode I, II and III). The decohesion of the interface was modelled using displacement-based damage CZM with bilinear traction-separation law. As aforementioned, the adhesion strength σ_c and fracture energy (energy release rate) G_c were yet to be decided. The tensile (mode I) and shear (mode II and III) values can be different for both the adhesion strength and fracture energy. However, in the current study, the tensile values are less significant compared to the shear ones, since the interface fracture is tangentially dominated. Therefore, major attention should be paid to the tangential/shear values, and the tensile values are just determined by use similar values as those found in the literature. Tab. 2 lists some values found in the literature. The tensile strength ranged between 0.15 and 1.3 MPa, and mode-I fracture energy varied from 0.2 to 9 J/m^2. The final values chosen for σ_{ct} and G_{ct} were 1.1 MPa and 1J/m^2 respectively. They may not be accurate but these are reasonable approximations when concrete information is unavailable.

Apart from the cohesive properties, three mechanical properties of ice were also needed, namely, density ρ, Young’s modulus E, and Poisson’s ratio ν. Values from literature were chosen, at 870 kg/m^3, 9000 MPa and 0.31,

respectively.

Tab. 2 Cohesive properties of ice/aluminium interfaces found in the literature

Author, date	σ_{ct} (MPa)	σ_{cs} (MPa)	G_{ct} (J/m^2)	G_{cs} (J/m^2)
Wei, 1996 [21] [1]	-	-	1	1
Pervier, 2012 [39] [1,*]	0.6 - 1.3 (Ice/Ti)	2 - 13.6	1.83 - 9 (Ice/Ti)	1
Chen, 2018 [32] [2]	0.15	0.15	0.2	0.2
Yavas, 2019 [18] [1]	-	0.4 (Lap shear)	-	0.25 (Lap shear)
	-	1.3 (push-out)	-	0.25 (push-out)
Dawood, 2020 [40] [1]	-	0.27 (Lap shear)	0.56	0.48 (Lap shear)

[1] Results from experiment.

[2] Results by fitting numerical prediction with experimental measurement.

* σ_{ct} and G_{ct} measured at LWC = 0.4 g/m^3, -20 ºC≤T≤-3 ºC. G_{cs} not given in the paper but a value of 1 J/m^2 used in FEA.

The mesh used for the computation is shown in Fig. 7. Fine mesh was used in ice domain, especially at the edge where crack was initiated and at the

interface where fracture occurred. On the other hand, the pipe was coarsely meshed because small variations of stresses were found there. A mesh independent study was performed, and the final mesh contained a total number of around 4500 elements. A Time-dependent (Transient) study was performed and the incrementation of timestep of 0.01 s was proved to be sufficient.

To determine the adhesive shear strength σ_{cs} and shear energy release rate G_{cs}, the force needed to detach the ice predicted by FEA must match the measured ones. The matching process is schematically illustrated in Fig. 8. It begins with a choice of critical shear strength σ_{cs} based on previous studies. Next, the applied pushing force can be set to vary with time $F = f(t)$. The function $f(t)$ can be approximated as a linear type whose slope can be determined according to the loading rate of the test. Then, different values for G_{cs} can be tried, and the simulation is run. The instant of fracture, t_f, is the moment when the maximum damage factor reaches the value of 1. The numerically predicted critical force is therefore $F_{c,FEA} = f(t_f)$. A threshold of the difference between FEA and measured value of the critical force can be set, $\widetilde{\Delta F}$. If $\left|\frac{F_{c,FEA}-F_{c,measurment}}{F_{c,measurment}}\right| \leq \widetilde{\Delta F}$ holds, this run of FEA can be accepted. Otherwise, another value for G_{cs} is set, and run the FEA again. If no suitable value for G_{cs} can be found, then change the value for σ_{cs} and repeat the

entire process.

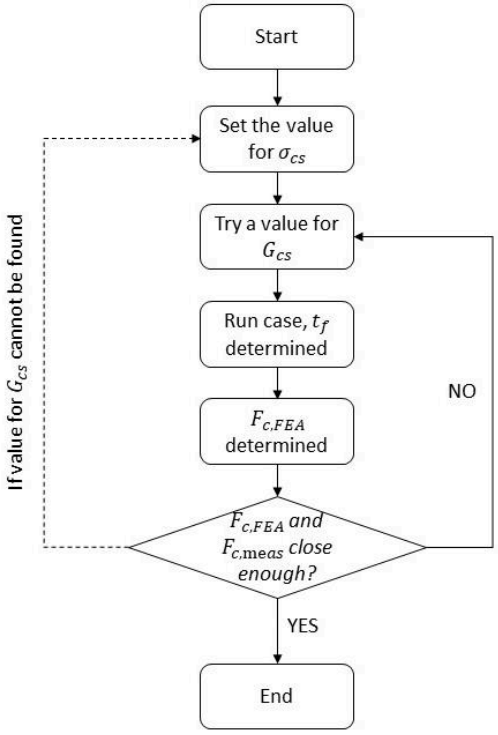

Fig. 8 Flowchart of the matching process

3.2 FEA result and discussion

The critical shear strength of the interface σ_{cs} is the maximum shear stress the interface can withstand when subjected to pure shear. Therefore, the higher σ_{cs} is, the more difficult the crack is to open. Fig. 9 shows the change of predicted fracture moment and critical force with the variation of the critical shear strength. It can be seen from the plot that for shear strength up to 1 MPa, the predicted fracture moment and the pushing force increased with the increase of shear strength. Beyond that, the growth of shear strength did not

influence the fracture time or the pushing force too much. This was because in the latter case the tensile strength became critical. In other words, for high values of σ_{cs}, the tensile strength σ_{ct} became the critical factor determining the fracture, while for low values of σ_{cs}, the shear strength was more significant. Similar trend was found in the influence of shear energy release rate, as is shown in Fig. 10. The matched point was marked both in Fig. 9 and Fig. 10. The numerically predicted shedding force was 65 N, corresponding to a critical force of $F_c = 65 \times 2 = 130\ N$ for the case of a complete geometry, which was close to the measurement, at 127 N. the matched shear strength σ_{cs} and mode-II energy release rate G_{cs} were 1 MPa and $1\ J/m^2$, respectively.

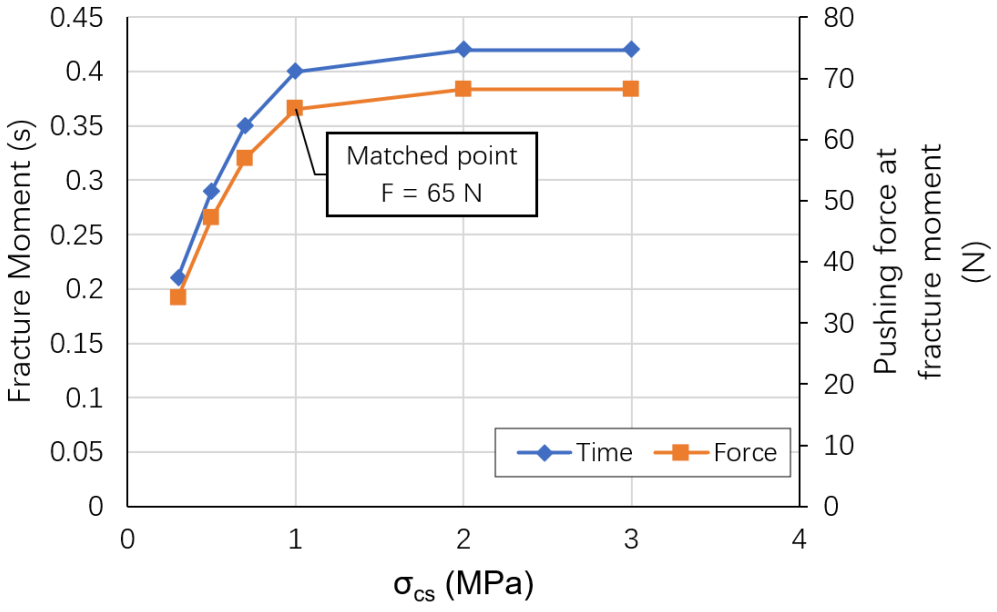

Fig. 9 Influences of critical shear strength on the fracture moment and critical force: $G_{cs} = 1\ J/m^2,\ \sigma_{ct} = 1.1\ MPa,\ G_{ct} = 1\ J/m^2$.

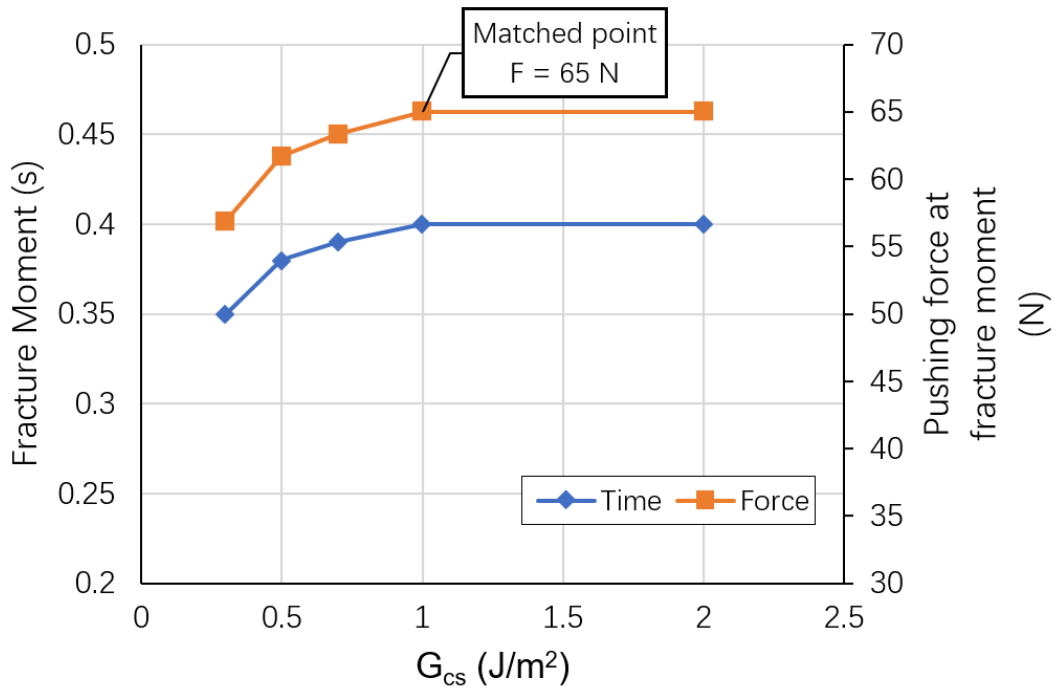

Fig. 10 Influences of shear energy release rate on the fracture moment and critical force: $\sigma_{cs} = 1\ MPa,\ \sigma_{ct} = 1.1\ MPa,\ G_{ct} = 1\ J/m^2$

The shedding moment can be determined by looking at the damage factor at the interface. A damage factor of 0 corresponds to no damage while the damage factor of 1 is for complete damage. Considering from the experimental data that the interface fracture occurred within a fraction of a second, it is reasonable to assume that once the damage factor reached 1 locally somewhere at the interface, a sudden fracture would follow immediately. At 0.1s, as expected, the damaged area was negligible, as shown in Fig. 11a; the shear stress across the interface was low. Stress concentration was found at the edge on which the force was applied but it was not sufficient to cause any damage. With the increase of the pushing force, the damaged area expanded

from the edge towards the interior of the interface. In the meantime, the peak of the shear stress also moved from the edge despite absence of any cracks. The maximum damage factor reached 1 at 0.4s which was the fracture moment. Further inspecting the contour revealed that the location where the damage factor reached 1 at the shedding moment was at the edge, while anywhere else it was lower than 1. The reason was that the edge was the region of stress concentration. By further increasing the force, the completely damaged area propagated quickly, and the shear stress peak continued moving downstream. By the time of 0.6 s, the damaged area took up more than 20 per cent of the entire interface. The ice may have shed from the pipe at this moment (in the experiment, ice shed at 0.4s), though the interface was not totally damaged. To better model ice shedding, CZM can be used in couple with other models. For example, a combination of CZM and extended finite element method (XFEM), for example, as presented in the paper by Fu et al. [31], could ensure a more accurate prediction.

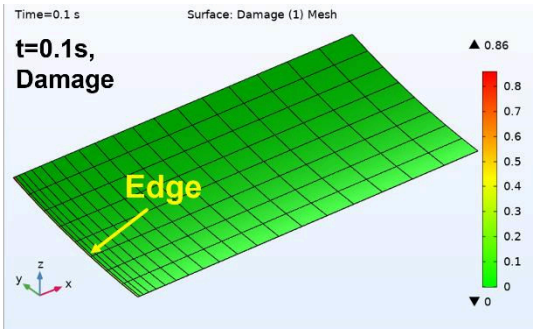

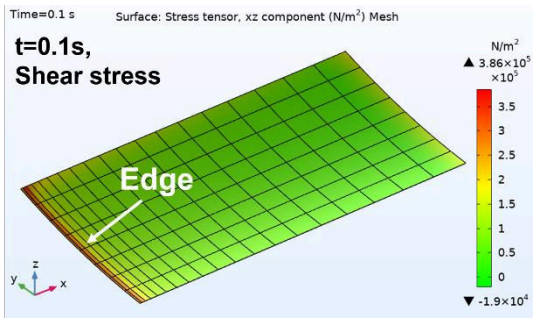

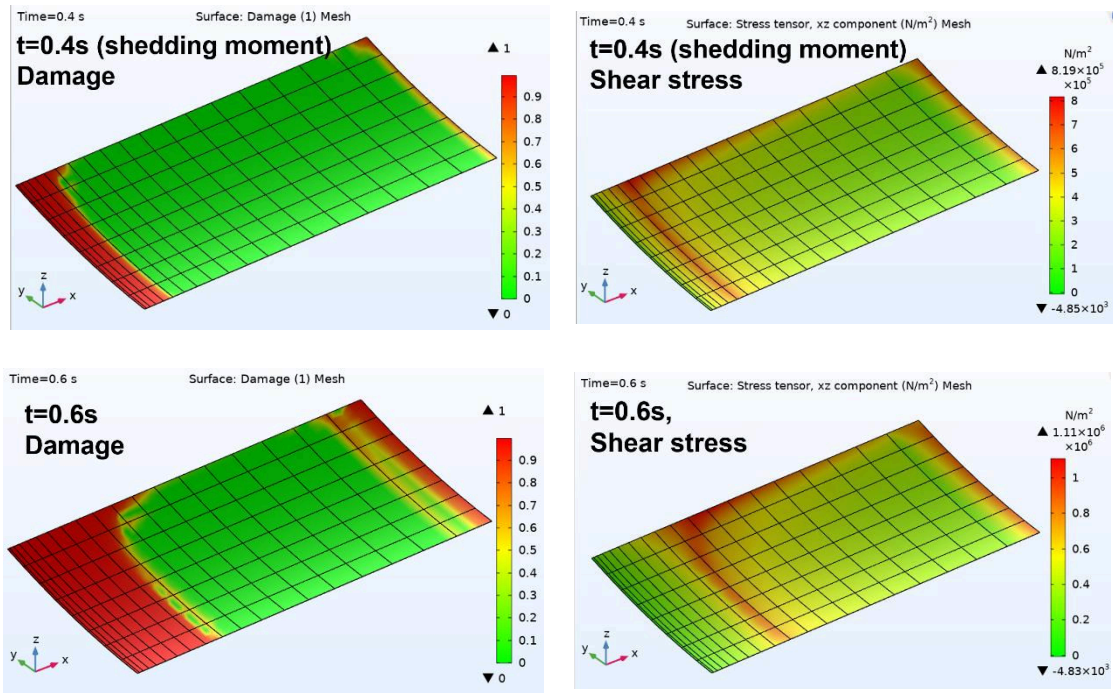

(a) Damage (b) Shear stress

Fig. 11 Damage progression (a) and shear stress evolution (b) at the interface. The damage factor reached 1 at 0.4s which was the shedding moment. The peak of the shear stress moved downstream as pushing force gradually increased.

Fig. 12 shows how the shear stress, the damage factor and the bilinear traction-separation law were interrelated. The contours of shear stress and damage factor were taken at the moment of fracture (0.4s). The peak of the shear stress coincided with the separation line between damaged and undamaged area, if all the edge effects were ignored. This was because the peak is the maximum stress the interface can withstand without incurring any damage. Due to stress concentration, the region on the left of the separation

line had experienced the maximum stress sometime before the shedding moment, causing damage to the interface therefore resulting in a drop in its ability to withstand stresses, as displayed in the plot on the right of Fig. 12. The interface was accordingly at the softening state. The stress on the right of the separation line was lower than the peak stress (damage threshold stress), and thus no damage was caused. The interface was therefore at the linear elastic state. Inside the softening area with a positive damage factor, the damage factor decreased from the edge all the way to the peak. At the moment of debonding (0.4 s), the damage factor at the edge was exactly at 1, meaning that the crack started to open at the edge. After this moment, the real crack propagated in positive x direction, leaving an area being totally damaged, as shown in Fig. 13.

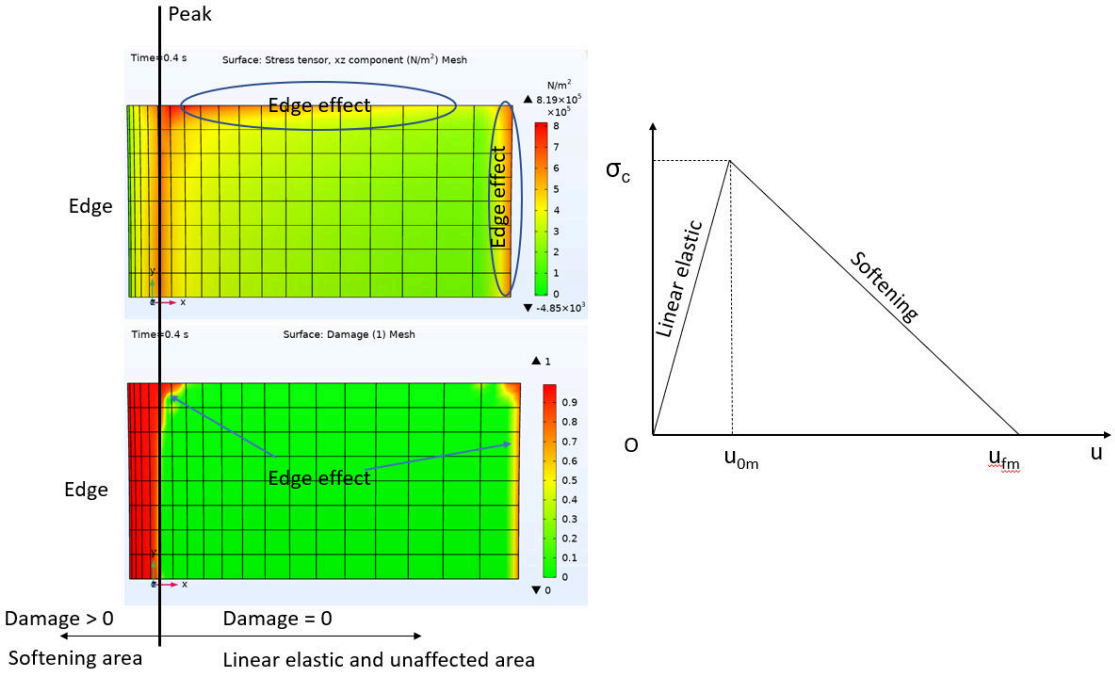

Fig. 12 The interrelationship among shear stress, damage factor and the traction-separation law

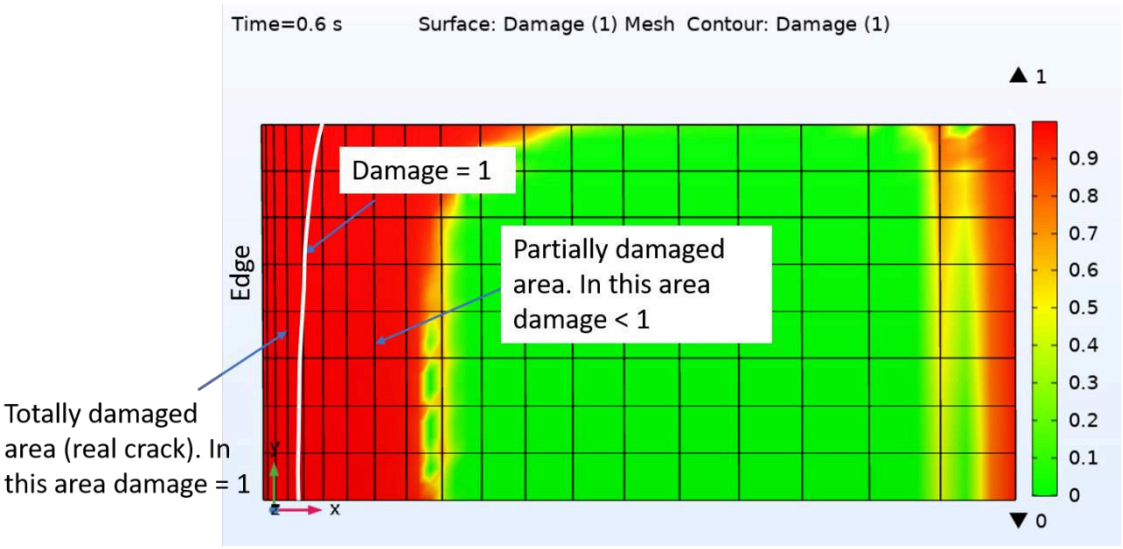

Fig. 13 The crack propagated from the edge to interior at 0.6 s.

The shear stress along the path at the moment of debonding is plotted in Fig. 14. The peak shear stress was found 1.6 mm away from the edge, at 0.634 MPa. It is clear from the graph that inside the undamaged area the shear stress increased almost exponentially when approaching the edge. However, inside the damaged area, the shear stress did not continue to rise to an infinity at the edge as expected but instead plummeted to 0. In other words, the shear stress was not accurately predicted in the damaged area. The reason, again, is that the CZM is nonphysical. Inside the damaged area, CZM assumed that the stresses decrease with the increase of separation, and therefore a sharp drop was found in the plot. The peak shear stress was equivalent to the local

adhesive shear strength of the ice/pipe interface. The value found (0.634 MPa) was lower than the value for shear strength σ_{cs} we assigned for the cohesive property which was at 1 MPa. This is because mode-I fractures also played a role at the interface, although the force exerted was purely shear.

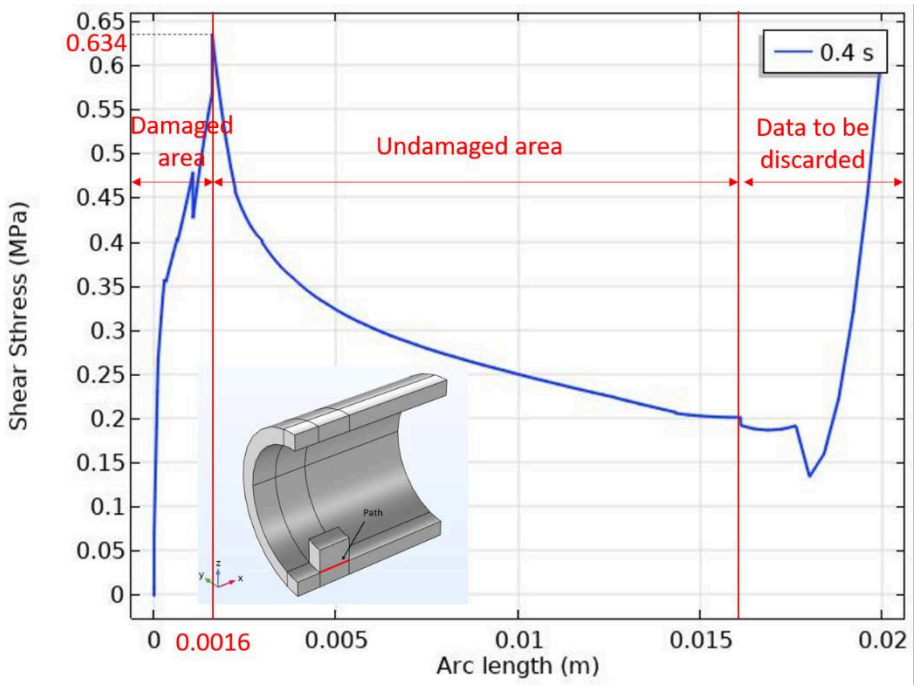

Fig. 14 Shear stress distribution along the path at the moment of fracture

Up to this point, whether the interface debonding is strength-controlled or toughness-controlled still remains unknown. According to Golovin et al. [17], if the interface strength controls the debonding, the average shear strength $\sigma_{s,avg} = F_c/A$ would be the true shear strength σ_{cs}. Whereas, if the debonding is toughness-controlled, σ_{cs} cannot be directly measured and is irrelevant to the interface length. Ignoring the curvature of the ice/pipe interface and assuming the interface deforms linear-elastically under pure shear, the critical

force can be determined by [17]:

$$= \sqrt{2G_{cs}E}\left(\frac{1-e^{-2\omega l}}{1+e^{-2\omega l}}\right) \quad (3)$$

where, G_{cs} is the critical shear energy, E is the modulus of ice, and are the width, height and length of the ice block, respectively, and,

$$= \frac{F_c}{} \quad (4)$$

$$\omega = \frac{\sigma_{cs}}{\sqrt{2G_{cs}}} \quad (5)$$

For sufficiently long interfaces ($l \to \infty$),

$$= \sqrt{2G_{cs}E} \quad (6)$$

which means that the critical force is decided only by fracture energy G_{cs}.

For short interfaces,

$$\frac{1-e^{-2\omega l}}{1+e^{-2\omega l}} \approx \omega l \quad (7)$$

thus,

$$= \omega l\sqrt{2G_{cs}Eh} = \sigma_{cs} l \quad (8)$$

which means that critical force is proportional to the length of the ice block.

To verify the theory, a parametric study on the influence of interface length on the critical force was performed. For each FEA case, all dimensions remained unchanged except the length of the ice block. A range of lengths from 10 to 50 mm were studied. The cohesive properties of ice used for the theoretical model were those matched with the measurement, namely, $\sigma_{cs} = 1\,MPa$, $G_{cs} = 1\,J/m^2$, $\sigma_{ct} = 1.1\,MPa$, $G_{ct} = 1\,J/m^2$. Dimensions of ice block and the interface can be found in Fig. 7. The FEA results were compared to that calculated from theory (Eq. 3) in Fig. 15. The FEA plot showed the same asymptotic trend as that of the theory, changing linearly for short lengths and approaching the asymptotic value for long lengths. The FEA made a good prediction – approximately 40 mm – on the critical length l_c defined as the specific length beyond which the interface debonding will be toughness-controlled. Critical forces calculated from Eq. 3 were however much higher than the numerically predicted counterparts. One important reason is that the theoretical model completely ignored the mode-I fracture which could play a critical part in the interface delamination, although the push is totally tangential.

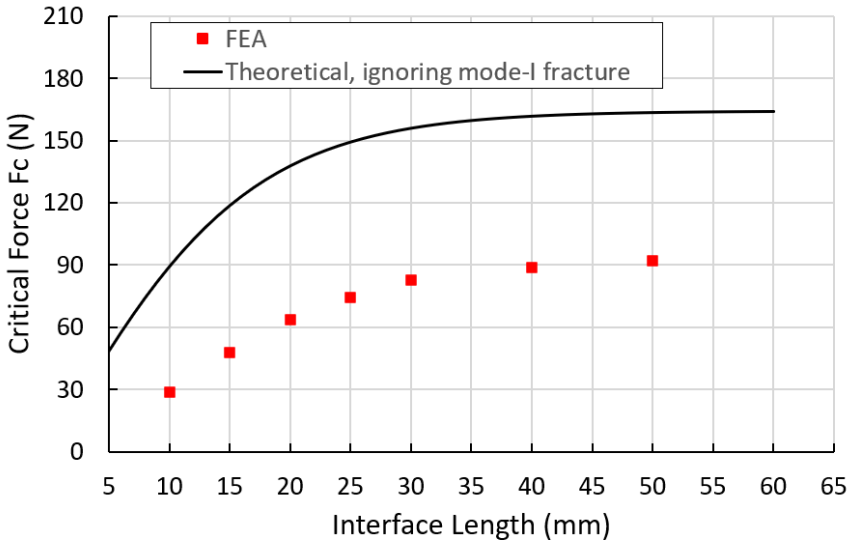

Fig. 15 Change of critical forces with interface length, a comparison between FEA and theoretical results.

4 Conclusion

A combined study of experiment and FEA was performed to obtain the adhesive shear strength and fracture energy of the interface between ice and cylindric surfaces of an aluminium pipe. The measured critical force was at 127 N which corresponded to an average shear strength of 317.5 kPa. The entire shedding process took about 0.4 s to complete, and the corresponding loading rate was calculated to be at $317.5\ N/s$. The true adhesive shear strength σ_{cs} and mode-II fracture energy G_{cs} were determined, at 1MPa and 1 J/m^2 respectively, through an iterative process of matching the numerically predicted critical force to the measurement. The FEA revealed that the shear stress peak propagated from the edge where stress concentration existed

toward to the interior of the interface as the push increased, and it coincided with the boundary separating damaged and undamaged areas. The FEA made a good prediction on the trend of the change of critical force with interface length, but underpredicted its absolute magnitude. The reason might be that the theoretical model completely ignored the mode-I fracture which could play a critical part in the interface delamination.

Acknowledgement

This project has received funding from the Clean SKY JTI within the European Union´s Horizon 2020 research and innovation programme under grant agreement No. 821301.

References

[1] Green, S. D. (2006) 'A study of U. S. inflight icing accidents and incidents, 1978 to 2002', in *Collection of Technical Papers - 44th AIAA Aerospace Sciences Meeting*, pp. 1048–1073. doi: 10.2514/6.2006-82.

[2] Appiah-Kubi, P., Martos, B., Atuahene, I. and William, S. (2013) 'U.S. inflight icing accidents and incidents, 2006 to 2010', *IIE Annual Conference and Expo 2013*, 4000.

[3] Cao, Y., Tan, W. and Wu, Z. (2018) 'Aircraft icing: An ongoing threat to aviation safety', *Aerospace Science and Technology*. Elsevier Masson SAS, pp. 353–385. doi: 10.1016/j.ast.2017.12.028.

[4] Work, A. and Lian, Y. (2018) 'A critical review of the measurement of ice adhesion to solid substrates', *Progress in Aerospace Sciences*. Elsevier Ltd, 98(March), pp. 1–26. doi: 10.1016/j.paerosci.2018.03.001.

[5] Laforte, C. and Beisswenger, A. (2005) 'Icephobic Material Centrifuge Adhesion Test', *Proceedings of the International Workshop on Atmospheric Icing of Structures (IWAIS XI)*, (June), pp. 1–5. Available at: https://www.researchgate.net/publication/260019223 (Accessed: 28 July 2020).

[6] Fortin, G., Beisswenger, A. and Perron, J. (2010) 'Centrifuge adhesion tests to evaluate icephobic coatings', in *AIAA Atmospheric and Space Environments Conference 2010*. Reston, Virigina: American Institute of Aeronautics and Astronautics. doi: 10.2514/6.2010-7837.

[7] Rønneberg, S., Laforte, C., Volat, C., He, J. and Zhang, Z. (2019) 'The effect of ice type on ice adhesion', *AIP Advances*. American Institute of Physics Inc., 9(5), p. 055304. doi: 10.1063/1.5086242.

[8] Loughborough, D. L. and Haas, E. G. (1946) 'Reduction of the Adhesion of Ice to De-Icer Surfaces', *Journal of the Aeronautical Sciences*, 13(3), pp. 126–134. doi: 10.2514/8.11328.

[9] Fortin, G. and Perron, J. (2009) 'Spinning Rotor Blade Tests in Icing Wind Tunnel', in *1st AIAA Atmospheric and Space Environments Conference*. Reston, Virigina: American Institute of Aeronautics and Astronautics, pp. 22–25. doi: 10.2514/6.2009-4260.

[10] Brouwers, E. W., Palacios, J. L., Smith, E. C. and Peterson, A. A. (2010) 'The experimental investigation of a rotor hover icing model with shedding', in *Annual Forum Proceedings - AHS International*, pp. 1157–1173.

[11] Pervier, M. L. A., Gurrutxaga Lerma, B., Piles Moncholi, E. and Hammond,

D. W. (2019) ‘A new test apparatus to measure the adhesive shear strength of impact ice on titanium 6Al-4V alloy’, *Engineering Fracture Mechanics*. Elsevier Ltd, 214, pp. 212–222. doi: 10.1016/j.engfracmech.2019.01.039.

[12] Druez, J., Phan, C. L., Laforte, J. L. and Nguyen, D. D. (1978) ‘Adhesion of glaze and rime on aluminium electrical conductors’, *Transactions of the Canadian Society for Mechanical Engineering*. Transactions of the Canadian Society for Mechanical Engineering, 5(4), pp. 215–220. doi: 10.1139/tcsme-1978-0033.

[13] Dong, W., Ding, J. and Zhou, Z. X. (2014) ‘Experimental Study on the Ice Freezing Adhesive Characteristics of Metal Surfaces’, *Journal of Aircraft*. American Institute of Aeronautics and Astronautics Inc., 51(3), pp. 719–726. doi: 10.2514/1.C032393.

[14] Scavuzzo, R. J. and Chu, M. L. (1987) ‘Structural Properties of Impact Ices Accreted on Aircraft Structures’, *Nasa-Cr-179580*, (January 1987).

[15] Kraj, A. G. and Bibeau, E. L. (2010) ‘Measurement method and results of ice adhesion force on the curved surface of a wind turbine blade’, *Renewable Energy*. Pergamon, 35(4), pp. 741–746. doi: 10.1016/j.renene.2009.08.030.

[16] Meuler, A. J., Smith, J. D., Varanasi, K. K., Mabry, J. M., McKinley, G. H.

and Cohen, R. E. (2010) ‘Relationships between water wettability and ice adhesion’, *ACS Applied Materials and Interfaces*. American Chemical Society, 2(11), pp. 3100–3110. doi: 10.1021/am1006035.

[17] Golovin, K., Dhyani, A., Thouless, M. D. and Tuteja, A. (2019) ‘Low-interfacial toughness materials for effective large-scale deicing’, *Science*. American Association for the Advancement of Science, 364(6438), pp. 371–375. doi: 10.1126/science.aav1266.

[18] Yavas, D., Bastawros, A., Dawood, B. and Giuffre, C. (2019) ‘Characterization of Mode-II Interfacial Fracture Toughness of Ice/Metal Interfaces’, in *SAE Technical Papers*, pp. 1–5. doi: 10.4271/2019-01-1947.

[19] Raraty, L. E. and Tabor, D. (1958) ‘The adhesion and strength properties of ice’, *Proceedings of the Royal Society of London. Series A. Mathematical and Physical Sciences*. The Royal Society, 245(1241), pp. 184–201. doi: 10.1098/rspa.1958.0076.

[20] Petrenko, V. F. and Peng, S. (2003) ‘Reduction of ice adhesion to metal by using self-assembling monolayers (SAMs)’, *Canadian Journal of Physics*. NRC Research Press Ottawa, Canada, 81(1–2), pp. 387–393. doi: 10.1139/p03-014.

[21] Wei, Y., Adamson, R. M. and Dempsey, J. P. (1996) *Ice/metal interfaces: fracture energy and fractography*, *JOURNAL OF MATERIALS SCIENCE*. Springer Netherlands. doi: 10.1007/BF00352894.

[22] Ashby, M. F., Gandhi, C. and Taplin, D. M. R. (1979) 'Overview No. 3 Fracture-mechanism maps and their construction for f.c.c. metals and alloys', *Acta Metallurgica*. Pergamon, 27(5), pp. 699–729. doi: 10.1016/0001-6160(79)90105-6.

[23] Ashby, M. F. and Hallam (Née Cooksley), S. D. (1986) 'The failure of brittle solids containing small cracks under compressive stress states', *Acta Metallurgica*. Pergamon, 34(3), pp. 497–510. doi: 10.1016/0001-6160(86)90086-6.

[24] Cottrell, A. H. (1989) 'Strengths of grain boundaries in pure metals', *Materials Science and Technology*, 5(12), pp. 1165–1167. doi: 10.1179/mst.1989.5.12.1165.

[25] Sutton, A. P. (1995) 'Interfaces in crystalline materials', *Monographs on the Physice and Chemistry of Materials*. Clarendon Press, pp. 414–423.

[26] Pervier, M. A., Pervier, H. and Hammond, D. W. (2017) 'Observation of microstructures of atmospheric ice using a new replica technique', *Cold*

Regions Science and Technology. Elsevier B.V., 140, pp. 54–57. doi: 10.1016/j.coldregions.2017.05.002.

[27] Dawood, B., Giuffre, C. and Bastawros, A. (2018) 'Fracture Mechanics Based Approach for Ice Adhesion Characterization', in *2018 Atmospheric and Space Environments Conference*. Reston, Virginia: American Institute of Aeronautics and Astronautics, pp. 1–11. doi: 10.2514/6.2018-3343.

[28] Pervier, M. L. A. and Hammond, D. W. (2019) 'Measurement of the fracture energy in mode I of atmospheric ice accreted on different materials using a blister test', *Engineering Fracture Mechanics*. Elsevier, 214(February), pp. 223–232. doi: 10.1016/j.engfracmech.2019.02.003.

[29] Zarasvand, K. A., Mohseni, M. and Golovin, K. (2021) 'Cohesive zone analysis of cylindrical ice adhesion: Determining whether interfacial toughness or strength controls fracture', *Cold Regions Science and Technology*. Elsevier B.V., 183, p. 103219. doi: 10.1016/j.coldregions.2020.103219.

[30] Chen, Y., Dong, W., Wang, Z. and Fu, L. (2015) 'Numerical simulation of ice shedding from a fan blade', in *Proceedings of the ASME Turbo Expo*. American Society of Mechanical Engineers, pp. 1–8. doi: 10.1115/GT2015-42265.

[31] Fu, L., Chen, Y., Xu, M., Wu, X. and Dong, W. (2016) 'Numerical Simulation of Ice Shedding From a Spinning Cone by Using Coupled CZM and XFEM', in *Volume 7A: Structures and Dynamics*. American Society of Mechanical Engineers. doi: 10.1115/GT2016-56854.

[32] Chen, Y., Fu, L. and Dong, W. (2018) 'Novel Cohesive/Adhesive Ice Shedding Model for Spinner Cone', *Journal of Propulsion and Power*, 34(3), pp. 647–659. doi: 10.2514/1.B36289.

[33] Chen, Y., Wenhao, W., Dong, W., Li, M. and Lei, L. (2014) 'Numerical study on the adhesion strength between ice and aluminium based on a cohesive zone model', in *Proceedings of the ASME Turbo Expo*. American Society of Mechanical Engineers (ASME). doi: 10.1115/GT2014-25171.

[34] Matbou Riahi, M., Marceau, D., Laforte, C. and Perron, J. (2011) 'The experimental/numerical study to predict mechanical behaviour at the ice/aluminium interface', *Cold Regions Science and Technology*. Elsevier, 65(2), pp. 191–202. doi: 10.1016/j.coldregions.2010.09.002.

[35] Schulz, M. and Sinapius, M. (2015) 'Evaluation of Different Ice Adhesion Tests for Mechanical Deicing Systems Methods of Ice Adhesion Strength Measurement', *SAE 2015 International Conference on Icing of Aircraft, Engines, and Structures*. doi: 10.4271/2015-01-2135.Copyright.

[36] Vincent, A., Pervier, H., Pervier, M., Nalianda, D. and Protection, I. (2020) 'Experimental setup to measure and analyze ice adhesion on air cycle machine turbine exit pipe surface', in *Aerospace Europe Conference 2020*. Bordeaux.

[37] Rønneberg, S., Zhuo, Y., Laforte, C., He, J. and Zhang, Z. (2019) 'Interlaboratory Study of Ice Adhesion Using Different Techniques', *Coatings*. MDPI AG, 9(10), p. 678. doi: 10.3390/coatings9100678.

[38] Chu, M. C. and Scavuzzo, R. J. (1991) 'Adhesive shear strength of impact ice', *AIAA Journal*, 29(11), pp. 1921–1926. doi: 10.2514/3.10819.

[39] Pervier, M.-L. (2012) 'Mechanics of Ice Detachment Applied To Turbomachinery', *PhD thesis*, pp. 1–183.

[40] Dawood, B., Yavas, D., Giuffre, C. J. and Bastawros, A. (2020) 'Characterization of Ice Adhesion: Approaches and Modes of Loading', in *AIAA AVIATION 2020 FORUM*. Reston, Virginia: American Institute of Aeronautics and Astronautics, pp. 1–12. doi: 10.2514/6.2020-2802.

Author Statement

An Feng: Methodology, Validation, Formal analysis, Data Curation, Writing - Original Draft, Visualization.

Abhay Vincent: Investigation.

ML.A. Pervier: Conceptualization, Resources, Writing - Review & Editing, Supervision

Declaration of interests

☒ The authors declare that they have no known competing financial interests or personal relationships that could have appeared to influence the work reported in this paper.

☐The authors declare the following financial interests/personal relationships which may be considered as potential competing interests:

Highlights

- A new push test to measure average adhesive shear strength of ice on curved surface
- Peak shear strength and fracture energy obtained by matching FEA and measurement
- Stress distribution and crack propagation on ice/Al interface provided by FEA
- Good agreement between critical length predicted by theory and Finite Element Model

https://dspace.org/

Measurement and FEM of ice adhesion to the downstream pipe of an air cycle machine

Feng, An; Vincent, Abhay; Pervier, Marie Laure A.

2022-04-01
Elsevier
https://doi.org/10.1016/j.coldregions.2022.103512
Feng A, Vincent A, Pervier MLA. (2022) Measurement and FEM of ice adhesion to the downstream pipe of an air cycle machine. Cold Regions Science and Technology, Volume 196, April 2022, Article number 103512

Downloaded from a DSpace repository. https://dspace.org/